Supporting Information for "*Ab initio* Quantum Simulation of Strongly Correlated Materials with Quantum Embedding"

Changsu Cao,[1,2] Jinzhao Sun,[3] Xiao Yuan,[4,5]
Han-Shi Hu,[2] Hung Q. Pham,[6,*] and Dingshun Lv[1,†]

[1]*ByteDance Inc, Zhonghang Plaza, No. 43, North 3rd Ring West Road, 100098 Beijing, China.*

[2]*Department of Chemistry, Tsinghua University, Beijing 100084, China*

[3]*Clarendon Laboratory, University of Oxford, Oxford OX1 3PU, United Kingdom*

[4]*Center on Frontiers of Computing Studies, Peking University, Beijing 100871, China*

[5]*School of Computer Science, Peking University, Beijing 100871, China*

[6]*ByteDance Inc, Mountain View, CA 94041, US.*

[*] hung.pham@bytedance.com

[†] lvdingshun@bytedance.com

I. COMPUTATIONAL DETAILS

The DMET workflow was implemented based on the package libDMET [1, 2]. The classical calculations of FCI, CCSD and HF were performed by using PySCF in this work [3, 4]. GTH pseudopotentials were employed to replace core electrons [5, 6]. The GTH-SZV basis set was used to represent the valence electron of H (1s) while GTH-DZVP-MOLOPT-SR basis sets were used for B, N, O, and Ni [7]. These correspond to 2s2p3s3p3d AOs for B, N, O and 3s3p3d4s4p4d4f5s AOs for Ni. Gaussian density fitting (GDF) was applied to evaluate the two-electron integrals [8]. An even-tempered Gaussian basis set was used as the auxiliary basis set with the exponential factor $\beta = 2.0$ for 1D-H and $\beta = 2.3$ for 2D-hBN and 3D-NiO [9]. The quantum simulations of embedding were performed by virtual quantum simulators on classic devices. The detailed implementation can be found according to Data Availability section. Yao [10] was used as the backend of QC solver when simulating 1D-H and 2D-hBN. For the larger simulations of NiO, Fermionic Quantum Emulator (FQE) [11] was chosen as the backend of QC solver to speed up the numerical calculations. The noisy simulations were based on the QASM simulator from Qiskit toolkit [12]. To mitigate quantum noise, the quantum observable is measured at noise-scaled quantum circuits by unitary folding and extrapolated to the zero-noise limit by linear fit supported by Mitiq package [13]. The scaling factors are 1.00, 1.25 and 1.50 in this work.

The momentum space was sampled using a Γ-centered Monkhorst-Pack grid. For 1D-H, 10 Å vacuum region was set to avoid interactions between the neighboring layers due to periodic boundary conditions. A $1\times1\times N_k$ **k**-mesh with N_k = 3, 5, 7, 9, 11 was studied. Similarly for h-BN, a 20.0 Å vacuum region was used to model the single layer structure. We employed three expanding **k**-meshes, *i.e.*, 5×5×1, 6×6×1, and 7×7×1. For NiO, both FM and AFII states are calculated using the lattice parameter $a = 4.17$ Å from the experiment [14]. The **k**-point of 2×2×2, 3×3×3 and 4×4×4 were employed, however, only the latter two were used to extrapolate the energy gaps to the thermodynamic limit (TDL). This two-point TDL extrapolation was reported to give good agreements with experimental measurements on silicon and carbon crystal [15]. For a non-embedding reference, we were only able to perform the **k**-sampled periodic CCSD (**k**-CCSD) calculation at the 2×2×2 **k**-point due to the current limitation of the computational resources.

The spin density in Fig. 2 is populated in Mulliken way [16] that the off-diagonal terms in

the one-particle reduced density matrix is equally attributed to the corresponding orbitals. The spin density of atom x is defined as difference of spin-up and spin-down electron density of atom x, which is expressed as

$$\rho_x = \sum_{i \subset x} (D_{ii,\alpha} - D_{ii,\beta}) + \frac{1}{2} \sum_{i \subset x, j \not\subset x} (D_{ij,\alpha} - D_{ij,\beta}), \tag{1}$$

where D is the one-particle reduced density matrix.

II. EXTRAPOLATION TO THERMODYNAMIC LIMIT OF 1D-H CHAIN

We performed DMET calculations of 1D hydrogen chain with different k-meshes, ranging from 1x1x5 to 1x1x45. Both the antiferromagnetic state (AFM) and the non-spin polarized state (NSP) have been calculated. The bond distance that the ground state transferring from NSP to AFM is shown in Fig. S1.

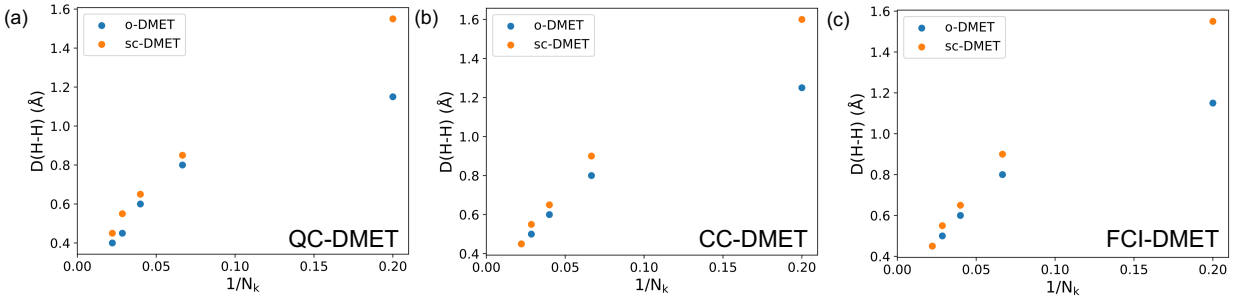

Fig. S1. The reciprocal k-point number vs. bond distance at which the ground state changes, as calculated by three different methods: (a) QC-DMET, (b) CC-DMET, and (c) FCI-DMET.

According to Fig. S1, the DMET calculation with solvers predict similar bond distances of phase transition. We find that the predicted bond distance of sc-DMET is slightly larger than that of o-DMET. Our results are in agreement with previous studies, such as Liu et al. [17] and Motta et al. [18]. As a detailed example, we focus on the result of QC-DMET. Liu et al. [17] predicted the AFM state transfers at the range of 0.5-0.75 $\mathring{A}$ via AFQMC on hydrogen chain with the total number of atom N=50, which is consistent with the sc-DMET results (0.65 $\mathring{A}$, $N_k = 1/25$). Similarly, Motta et al. [18] predicted the phase transition at 0.85 $\mathring{A}$ using AFQMC, VMC and DMC with number of hydrogen atoms N=40, which is, however, slightly larger than the value, *ca.* 0.69 $\mathring{A}$ ($N_k = 1/20$), from the linear

extrapolation of sc-DMET in Fig. S1(a). Overall, our results demonstrate consistency with previous studies.

III. THE ENERGY DIFFERENCES OF 1D-H

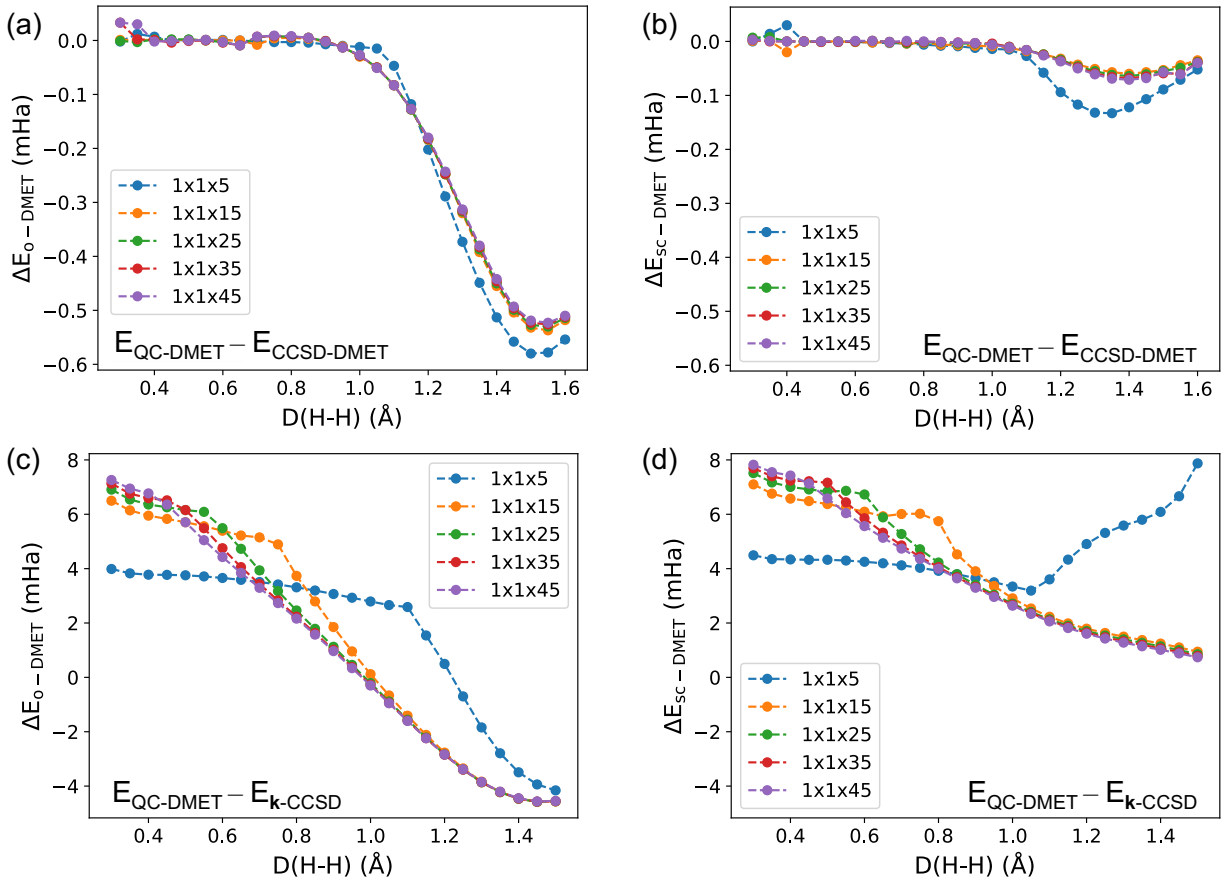

Fig. S2. Energy differences of (a) o-DMET (QC solver vs CCSD solver), (b) sc-DMET (QC solver vs CCSD solver), (c) o-DMET (QC solver) vs k-CCSD (no embedding), and (d) sc-DMET (QC solver) vs k-CCSD (no embedding) calculations, plotted against H-H bond distance. Ground state of each dot in figure refers to result of QC-DMET as different methods predict different phase transition bond distance. The same scale of vertical axis is used for the sub-figures in the same row.

To determine the accuracy and reliability of our QC solver, we compare its energy differences with other results in Fig. S2. We find that the energy difference between our QC solver and CCSD solver is less than 1 mHa for all bond distances studied. For both o-DMET

and sc-DMET, the energy difference increases as the bond dissociates. The energy difference for sc-DMET is particularly small in the dissociation zone. The agreement between our QC solver and CCSD solver improves as the k-mesh becomes denser. When comparing with **k**-CCSD results without embedding (shown in Fig. S2), we find that the deviation caused by embedding is larger than the energy difference among different solvers used in the DMET calculation. For o-DMET with our QC solver, the energy is several milli-Hartrees higher than the results of **k**-CCSD in the compressed zone and lower in the more stretched zones. After incorporating correlation potential fitting (sc-DMET), we observe that the energy difference in the compressed region remains small, but is significantly reduced by the self-consistent fitting of the correlation potential, particularly around the stretched region where D(H-H) $\geq$ 1.0 Å.

IV. THE ENERGY DIFFERENCES BETWEEN THE FM AND AFII STATE FOR NIO

The exchange coupling constants J_1 (nearest-neighbor) and J_2 (next-nearest-neighbor) for NiO are defined as [19]

$$J_1 = \frac{1}{16}(\mathrm{E_{AFI}} - \mathrm{E_{FM}}), \quad J_2 = \frac{1}{48}(4\mathrm{E_{AFII}} - 3\mathrm{E_{AFI}} - \mathrm{E_{FM}}) \tag{2}$$

where $\mathrm{E_{AFI}}$, $\mathrm{E_{AFII}}$, and $\mathrm{E_{FM}}$ are the energy of the AFI, AFII, and FM state, respectively. Thus, the energy differences between the FM and AFII state can be calculated as

$$\mathrm{E_{FM}} - \mathrm{E_{AFII}} = -12 \times (J_1 + J_2) \tag{3}$$

V. QUANTUM NOISY SIMULATIONS

The noisy quantum simulations are performed by introducing the effect of measurement shots and depolarizing noise to evaluate the performance of this method in more realistic conditions.

The noisy simulations are performed on closed-shell 1D hydrogen chain with GTH-SZV basis set. The distance between adjacent hydrogen atom is 1.5 Å. We choose a minimum fragment which contains one hydrogen atom due to the expensive computational cost when

TABLE S1. The energy differences between the FM and AFII state ($E_{FM} - E_{AFII}$ in meV/formula unit) for NiO from the literature.

Method	Ref.	J_1	J_2	$E_{FM} - E_{AFII}$
Exp.	[20]	-0.69	-8.66	112.2
Exp.	[21]	0.69	-9.51	105.8
HF	[22]	0.4	-2.3	22.8
LSDA+U	[23]	-0.03	-7.46	89.9
Fock35	[22]	0.95	-9.35	100.8
GGA+U	[24]	0.87	-9.54	104.0
LDA+U	[23]	0.01	-9.27	111.1
PBE	[25]	0.83	-9.47	103.7
B3LYP	[22]	1.2	-13.35	145.8
SIC-LMTO	[19]	0.9	-5.5	55.2
LSIC-LSDA	[26]	0.15	-6.92	81.2
LSIC-LSDA	[26]	1.42	-6.95	66.4
SIC-LSDA	[19]			116.0
SIC-LSDA (ES)	[19]			106.4

including measurements. The corresponding embedding thus contains 4 spin-orbitals and has the size of 4 qubits. Only chemical potential fitting is performed here.

We first consider only the fluctuation caused by finite shots without any gate noise involved. Here one shot represents a single execution of the quantum algorithm. Simulated results with the number of shots ranging from 2^{10} to 2^{20} are depicted in Fig. S3(a). The precision of the DMET energy improves and converges well as the increase of number of shots. The standard deviation becomes smaller than 1.0 mHa when the number of shots reaches 2^{18}. Since no extra gate noise is introduced, the mean value of DMET energies shows high accuracy and the difference from the ideal reference value is smaller than 1.0 mHa even with several thousands shots ($\sim 2^{12}$).

In the following, the depolarization noise is introduced in the DMET simulation. The

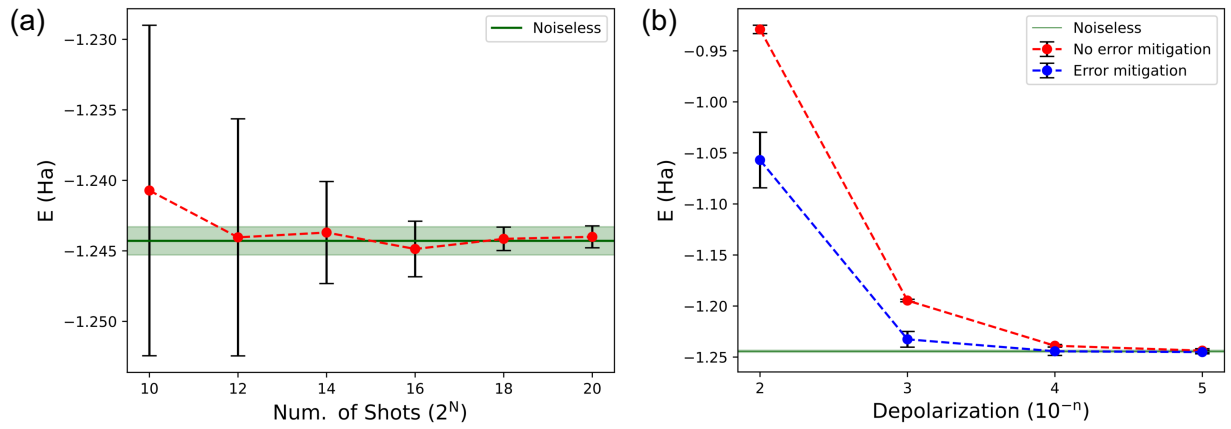

Fig. S3. (a) DMET energies vs. number of shots without extra gate noise. (b) DMET energies vs. depolarization probability with 2^{18} shots. The green line represents the noiseless reference calculated by numerical ideal solvers. The zone where the energy difference from the noiseless value is within 1.0 mHa has been marked by light green. Numerical experiments are repeated 10 times for each dot to get the mean and standard deviation.

depolarization noise is one of the most commonly used noise model in quantum simulations. By applying the depolarization noise model, there may be a bit-flip (Pauli **X** error) or a phase-flip (Pauli **Z** error) or both (Pauli **Y** error) to the input state based on the depolarizing probability p, when executing an operation in the quantum circuit [27, 28]. As shown in Fig. S3(b), the depolarizing noise leads to less accurate DMET energies while the standard deviation is just slightly affected by it. By applying the zero-noise extrapolation of linear fit, the more accurate results can be obtained at the expense of larger standard deviation. This worse precision after error mitigation is attributed to the deeper quantum circuit generated in the zero-noise extrapolation process.

In summary, the measurement shot mainly affects the precision while the depolarizing noise affects more the accuracy of the DMET results. The zero-noise extrapolation based on linear fit, which is one of the simplest error mitigation strategy, is used here to mitigate the quantum error. It improves the accuracy of the DMET energy while sacrificing the precision to some degree. It is a similar optimization procedure of chemical potential fitting, but more complex. We expect a good convergence achievable provided more robust error mitigation strategies and advanced sampling methods. Some recent studies show that the self-consistent quantum-classical hybrid algorithms remain well converged in the presence of

noise [29, 30]. Quantum error mitigation strategies such as zero-noise extrapolation [31, 32], stochastic methods [33, 34] and subspace expansion [35]. Besides that, reducing the depth of quantum circuit based on molecular symmetry [36] or in an adaptive manner [37, 38] can help to sample the observable with noise presented. Grouping commute Pauli terms can also reduce the cost of measurement for easier measurement (for example tensor product basis [39].

---

[1] Z.-H. Cui, T. Zhu, and G. K.-L. Chan, Efficient implementation of ab initio quantum embedding in periodic systems: Density matrix embedding theory, J. Chem. Theory Comput. **16**, 119 (2020).

[2] T. Zhu, Z.-H. Cui, and G. K.-L. Chan, Efficient formulation of ab initio quantum embedding in periodic systems: Dynamical mean-field theory, J. Chem. Theory Comput. **16**, 141 (2020).

[3] Q. Sun, X. Zhang, S. Banerjee, P. Bao, M. Barbry, N. S. Blunt, N. A. Bogdanov, X. Wang, A. White, and J. D. e. a. Whitfield, Recent developments in the pyscf program package, J. Chem. Phys. **153**, 024109 (2020).

[4] Q. Sun, T. C. Berkelbach, N. S. Blunt, G. H. Booth, S. Guo, Z. Li, J. Liu, J. D. McClain, E. R. Sayfutyarova, and S. e. a. Sharma, Pyscf: the python-based simulations of chemistry framework, Wiley Interdiscip. Rev. Comput. Mol. Sci. **8**, e1340 (2018).

[5] S. Goedecker, M. Teter, and J. Hutter, Separable dual-space gaussian pseudopotentials, Phys. Rev. B **54**, 1703 (1996).

[6] C. Hartwigsen, S. Goedecker, and J. Hutter, Relativistic separable dual-space gaussian pseudopotentials from H to Rn, Phys. Rev. B **58**, 3641 (1998).

[7] J. VandeVondele and J. Hutter, Gaussian basis sets for accurate calculations on molecular systems in gas and condensed phases, J. Chem. Phys. **127**, 114105 (2007).

[8] Q. Sun, T. C. Berkelbach, J. D. McClain, and G. K.-L. Chan, Gaussian and plane-wave mixed density fitting for periodic systems, J. Chem. Phys. **147**, 164119 (2017).

[9] G. L. Stoychev, A. A. Auer, and F. Neese, Automatic generation of auxiliary basis sets, J. Chem. Theory Comput. **13**, 554 (2017).

[10] X.-Z. Luo, J.-G. Liu, P. Zhang, and L. Wang, Yao.jl: Extensible, efficient framework for quantum algorithm design, Quantum **4**, 341 (2020).

[11] N. C. Rubin, K. Gunst, A. White, L. Freitag, K. Throssell, G. K.-L. Chan, R. Babbush, and T. Shiozaki, The Fermionic Quantum Emulator, Quantum **5**, 568 (2021).

[12] M. S. ANIS, Abby-Mitchell, H. Abraham, AduOffei, R. Agarwal, *et al.*, Qiskit: An open-source framework for quantum computing (2021).

[13] R. LaRose, A. Mari, S. Kaiser, P. J. Karalekas, A. A. Alves, P. Czarnik, M. E. Mandouh, M. H. Gordon, Y. Hindy, A. Robertson, P. Thakre, N. Shammah, and W. J. Zeng, Mitiq: A software package for error mitigation on noisy quantum computers, arXiv preprint arXiv:2009.04417 (2021).

[14] A. K. Cheetham and D. A. O. Hope, Magnetic ordering and exchange effects in the antiferromagnetic solid solutions $Mn_xNi_{1-x}O$, Phys. Rev. B **27**, 6964 (1983).

[15] J. McClain, Q. Sun, G. K.-L. Chan, and T. C. Berkelbach, Gaussian-based coupled-cluster theory for the ground-state and band structure of solids, J. Chem. Theory Comput. **13**, 1209 (2017).

[16] R. S. Mulliken, Electronic population analysis on lcao–mo molecular wave functions. i, J. Chem. Phys. **23**, 1833 (1955).

[17] Y. Liu, T. Shen, H. Zhang, and B. Rubenstein, Unveiling the finite temperature physics of hydrogen chains via auxiliary field quantum monte carlo, J. Chem. Theory Comput. **16**, 4298 (2020).

[18] M. Motta, C. Genovese, F. Ma, Z.-H. Cui, R. Sawaya, G. K.-L. Chan, N. Chepiga, P. Helms, C. Jiménez-Hoyos, A. J. Millis, U. Ray, E. Ronca, H. Shi, S. Sorella, E. M. Stoudenmire, S. R. White, and S. Zhang, Ground-state properties of the hydrogen chain: Dimerization, insulator-to-metal transition, and magnetic phases, Phys. Rev. X **10**, 031058 (2020).

[19] D. Ködderitzsch, W. Hergert, W. M. Temmerman, Z. Szotek, A. Ernst, and H. Winter, Exchange interactions in NiO and at the NiO(100) surface, Phys. Rev. B **66**, 064434 (2002).

[20] R. Shanker and R. A. Singh, Analysis of the exchange parameters and magnetic properties of NiO, Phys. Rev. B **7**, 5000 (1973).

[21] M. T. Hutchings and E. J. Samuelsen, Measurement of spin-wave dispersion in NiO by inelastic neutron scattering and its relation to magnetic properties, Phys. Rev. B **6**, 3447 (1972).

[22] I. de P. R. Moreira, F. Illas, and R. L. Martin, Effect of Fock exchange on the electronic structure and magnetic coupling in NiO, Phys. Rev. B **65**, 155102 (2002).

[23] S. Keshavarz, J. Schött, A. J. Millis, and Y. O. Kvashnin, Electronic structure, magnetism, and

exchange integrals in transition-metal oxides: Role of the spin polarization of the functional in DFT + U calculations, Phys. Rev. B **97**, 184404 (2018).

[24] F. J. Twagirayezu, Density functional theory study of the effect of vanadium doping on electronic and optical properties of NiO, Int. J. Comput. Mater. Sci. Eng. **08**, 1950007 (2019).

[25] Z. Rák and D. W. Brenner, Exchange interactions and long-range magnetic order in the $(\mathrm{Mg}, \mathrm{Co}, \mathrm{Cu}, \mathrm{Ni}, \mathrm{Zn})\mathrm{O}$ entropy-stabilized oxide: A theoretical investigation, J. Appl. Phys. **127**, 185108 (2020).

[26] G. Fischer, M. Däne, A. Ernst, P. Bruno, M. Lüders, Z. Szotek, W. Temmerman, and W. Hergert, Exchange coupling in transition metal monoxides: Electronic structure calculations, Phys. Rev. B **80**, 014408 (2009).

[27] Z. Babar, D. Chandra, H. V. Nguyen, P. Botsinis, D. Alanis, S. X. Ng, and L. Hanzo, Duality of quantum and classical error correction codes: Design principles and examples, IEEE Commun. Surv. Tutor. **21**, 970 (2019).

[28] B. M. Terhal, Quantum error correction for quantum memories, Rev. Mod. Phys. **87**, 307 (2015).

[29] Y. Liu, O. R. Meitei, Z. E. Chin, A. Dutt, M. Tao, T. Van Voorhis, and I. L. Chuang, Bootstrap embedding on a quantum computer (2023).

[30] J. Tilly, P. V. Sriluckshmy, A. Patel, E. Fontana, I. Rungger, E. Grant, R. Anderson, J. Tennyson, and G. H. Booth, Reduced density matrix sampling: Self-consistent embedding and multiscale electronic structure on current generation quantum computers, Phys. Rev. Research **3**, 033230 (2021).

[31] K. Temme, S. Bravyi, and J. M. Gambetta, Error mitigation for short-depth quantum circuits, Phys. Rev. Lett. **119**, 180509 (2017).

[32] Y. Li and S. C. Benjamin, Efficient variational quantum simulator incorporating active error minimization, Phys. Rev. X **7**, 021050 (2017).

[33] J. J. Wallman and J. Emerson, Noise tailoring for scalable quantum computation via randomized compiling, Phys. Rev. A **94**, 052325 (2016).

[34] J. Sun, X. Yuan, T. Tsunoda, V. Vedral, S. C. Benjamin, and S. Endo, Mitigating realistic noise in practical noisy intermediate-scale quantum devices, Phys. Rev. Applied **15**, 034026 (2021).

[35] X. Bonet-Monroig, R. Sagastizabal, M. Singh, and T. E. O'Brien, Low-cost error mitigation

by symmetry verification, Phys. Rev. A **98**, 062339 (2018).

[36] C. Cao, J. Hu, W. Zhang, X. Xu, D. Chen, F. Yu, J. Li, H.-S. Hu, D. Lv, and M.-H. Yung, Progress toward larger molecular simulation on a quantum computer: Simulating a system with up to 28 qubits accelerated by point-group symmetry, Phys. Rev. A **105**, 062452 (2022).

[37] H. R. Grimsley, S. E. Economou, E. Barnes, and N. J. Mayhall, An adaptive variational algorithm for exact molecular simulations on a quantum computer, Nat. Commun. **10**, 1 (2019).

[38] Y. Fan, C. Cao, X. Xu, Z. Li, D. Lv, and M.-H. Yung, Circuit-depth reduction of unitary-coupled-cluster ansatz by energy sorting, arXiv preprint arXiv:2106.15210 (2021).

[39] S. Bravyi, J. M. Gambetta, A. Mezzacapo, and K. Temme, Tapering off qubits to simulate fermionic hamiltonians (2017).